



Plasmonically induced transparency in in-plane isotropic and anisotropic 2D materials

SHENGXUAN XIA,^{1,2} XIANG ZHAI,¹ LINGLING WANG,¹ AND SHUANGCHUN WEN^{1,*}

¹Key Laboratory for Micro/Nano Optoelectronic Devices of Ministry of Education & Hunan Provincial Key Laboratory of Low-Dimensional Structural Physics and Devices, School of Physics and Electronics, Hunan University, Changsha 410082, China

²shengxuanxia@hnu.edu.cn

*scwen@hnu.edu.cn

Abstract: General two-dimensional (2D) material-based systems that achieve plasmonically induced transparency (PIT) are limited to isotropic graphene only through unidirectional bright–dark mode interaction. Moreover, it is challenging to extend these devices to anisotropic 2D films. In this study, we exploit surface plasmons excited at two crossed grating layers, which can be formed either by dielectric gratings or by the 2D sheet itself, to achieve dynamically tunable PIT in both isotropic and anisotropic 2D materials. Here, each grating simultaneously acts as both bright and dark modes. By taking isotropic graphene and anisotropic black phosphorus (BP) as proofs of concept, we reveal that this PIT can result from either unidirectional bright–dark or bidirectional bright–bright and bright–dark mode hybridized couplings when the incident light is parallelly/perpendicularly or obliquely polarized to the gratings, respectively. Identical grating parameters in isotropic (crossed lattice directions in anisotropic) layers produce polarization-independent single-window PIT, whereas different grating parameters (coincident lattice directions) yield polarization-sensitive double-window PIT. The proposed technique is examined by a two-particle model, showing excellent agreement between the theoretical and numerical results. This study provides insight into the physical mechanisms of PIT and advances the applicability and versatility of 2D material-based PIT devices.

© 2020 Optical Society of America under the terms of the [OSA Open Access Publishing Agreement](#)

1. Introduction

The use of surface plasmons (SPs)—the collective resonating waves of free charge carriers that are excited at metal–dielectric interfaces—is one of the most fundamental approaches to achieving strong light–matter interactions [1]. Because of their ability to confine an incident optical wave to its maximum size of one atom at the subwavelength scale [2], SPs can greatly enhance the local electromagnetic field in various types of metallic systems [3]. This paves the way for some important applications in areas such as sensing [2], waveguides [1], absorbers [4], and other optical modulators [5]. However, the lack of active tunability of its permittivities and the Ohmic and radiative losses of traditional metals at specific wavelengths has hindered the development of plasmon applications [1].

Compared to noble and traditional metals, the one-atom-thick graphene—a strictly two-dimensional (2D) crystal formed by honeycomb-structured carbon atoms—does not suffer from these types of problems in terahertz (THz) [2]. Owing to its fantastic thermal, optical, and mechanical properties, graphene offers an appropriate alternative for supporting plasmon resonances [6]. Triggered by the emergence of graphene as a unique platform for light–matter interactions, many studies have focused upon hundreds of other atomically thin 2D materials that retain their stability down to monolayers, such as transition metal oxides (TMOs) or dichalcogenides (TMDs), hexagonal boron nitride (hBN), and black phosphorus (BP) [7–10]. Because of their distinct properties of gapless or gapped band structures, or in-plane isotropic/anisotropic or hyperbolic

optical properties, these 2D materials have opened avenues for a variety of applications such as spintronics, catalysts, optical sensors, supercapacitors, and lithium-ion batteries [9]. In particular, these 2D materials have one key advantage, namely the ability to have their optical responses tuned actively via an external magnetostatic field, exposure to chemicals, and gating techniques [7,11]. This feature induces major improvements over conventional metallic plasmonics, making them a versatile conductive medium for the realization of a diverse range of active optical devices. Because of these unique properties, conductive 2D materials have become a versatile platform to support plasmon resonances and provide them with appealing properties such as electronic tunability, ultrastrong field confinement, and relative low damping [12,13]. Consequently, plasmons excited on these materials can provide an active platform for strongly enhanced light–matter interactions, triggering many novel functionalities and superior performance hitherto unavailable in conventional materials, such as light tunable absorption [14–17], optical modulation [9,18–21], photodetection [7], and sensing [12]. It also reveals some promising phenomena, such as nonlinearity [22], second-harmonic generations [23], and plasmonically induced transparency (PIT) [24,25]. As a consequence of the near-field coupled Fano interferences, the PIT process PIT is a classical analogue of electromagnetically induced transparency in plasmonic resonators between a ‘bright’ (superradiant, radiative) mode resonator, which is accessible from strong and direct coupling with incident light, and a ‘dark’ (subradiant, nonradiative) mode resonator, which is inaccessible (less-accessible) from (weak coupling with) incident light [26]. When these two resonators are brought together in both the spatial and frequency domains, their interference can generate a prominent window in an optical spectrum as they eliminate the resonant absorption in the system [27]. To achieve such coherent plasmonic interaction, localized surface plasmonic devices such as single-layer nanopatterned graphene [28,29] or BP [25], multilayer graphene sheets [24,30–32], and metal–graphene hybrid metamaterials [33] have been proposed. In recent years, these systems have greatly enriched the PIT phenomena through a lot of important plasmonics devices possessing high optical performance and wide tunability, including slow light effect [34], optical memory [35], and plasmonic sensors [24].

However, despite the ubiquitous presence of 2D material-based PIT effects, almost all of the relevant prior studies have focused only on the in-plane isotropic ones presented by graphene, little is known about the effects in anisotropic cases. Moreover, most of the PIT effects result from strong near-field one-way couplings from the superradiant (radiative/bright) mode to the subradiant (nonradiative/dark) mode, which in turn emerged from the breaking of the symmetry of the coupled system [26,28,33]. For this reason, the reported transparency windows in either solely material-based or two or more material-based hybridized PIT systems can be obtained using linearly polarized incident light at one or finitely many predefined directions to generate the bright mode [24,26,28,30,31,33], whereas totally polarization-independent PIT have rarely been proposed [32]. Moreover, owing to their geometry and structural symmetry, each of the coupled resonators is predetermined to work as bright (dark) mode, and cannot perform the role of the dark (bright) mode [24,26,28,30,31,33]. This has greatly weakened the active tunability of the 2D material-based PIT effect because the underlying physical concepts of a particular device only allows the existence of single-[26,28,31,33] or double-[36] window PIT.

In this work, we propose a double-layered grating structure formed by either dielectric gratings or the 2D material itself in crossed directions to achieve totally polarization-insensitive PIT on two layers of in-plane isotropic and anisotropic conductive 2D materials. Discussing all the types of 2D materials beyond the scope of this paper to discuss all the types of 2D materials, instead, graphene and BP have been taken as the proof of concept to illustrate some of the key characteristics of PIT for the isotropic and anisotropic cases, respectively. Using both analytical and numerical approaches, we examine how to achieve totally polarization-insensitive one-window PIT and polarization-sensitive two-window PIT for the two cases. We further prove that each layer of a 2D material can operate in either the bright or dark mode, or even both

simultaneously. These prominent characteristics of our proposed system serve to advance our understanding of the fundamental properties of PIT effect, and it is of great benefit to the design of 2D material-based PIT devices.

2. Methods

In this section, we introduce the methods and numerical model used in this study to develop the proposed structure. To focus on the proposed PIT effect resulted from the general optical responses of 2D materials, we restrict our model to classical electrodynamics and neglect any effects that may arise from the possible quantum finite-size effects, substrate phonons effects, and nonlinear effects since they are out of the research interest of our present study. The schematic of the proposed system is shown in Fig. 1. It comprises two periodic dielectric grating layers aligned along the x and y axes, respectively; furthermore, two layers of 2D material sheets covering a doped Si or SiO_2 conductor with refractive index n_3 and height d are between them. The upper-layer dielectric gratings (ULDGs) are periodically placed in the x direction and aligned infinitely along the y direction, while the lower-layer dielectric gratings (LLDGs) are rotated 90° with respect to the ULDGs. The dielectric constants, geometrical structure parameters, and optical conductivity of the materials are summarized in the Appendixes A and C. For the sake of simplicity, we assume that the system is surrounded by a uniform medium with an isotropic dielectric $n = 1$, unless specified otherwise. This setup is selected to help illuminate the fundamental nature of PIT and reveal the coupling mechanism between the two 2D material layers. This is a common assumption in many theoretical studies [2,37] as its simplicity does not alter the fundamental conclusions. In contrast to other metamaterial-based PIT systems, the proposed designs can avoid patterns of the 2D sheet; thus, the optical response of the structure is free of quantum finite-size and edge scattering effects (by zigzag and armchair boundary conditions) [37]. Technically, the proposed plasmonic system can be experimentally realized by utilizing recent etching techniques to fabricate layered grating devices with comparable, and even finer, geometrical parameters [38,39].

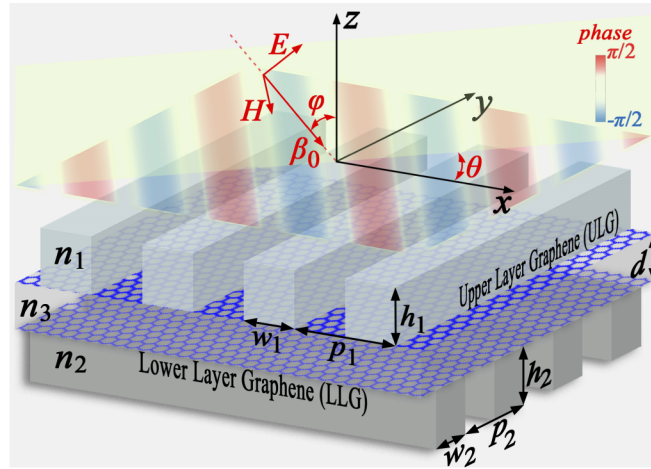


Fig. 1. Geometric configuration of the PIT system. Two layers of 2D material sandwiched between two periodic dielectric and crossed gratings are placed vertically along the z axis, which is inserted by a doped Si or SiO_2 conductor with refractive index n_3 and thickness d . The upper and lower gratings are designed with widths w_1 and w_2 , heights h_1 and h_2 , refractive indices n_1 and n_2 , and transverse periods p_1 and p_2 , respectively. A linearly polarized plane wave with wave vector β_0 and polarization angle θ relative to the x axis impinges the device at incident angle φ with respect to the z axis.

3. Results and discussion

3.1. Single-window PIT

In this section, we use graphene as an example to exploit the plasmonic excitation and coupling of the layered grating system and demonstrate the extraordinary single window PIT effect for the case of isotropic 2D materials. The reason to use gratings here is that gratings, either formed by attached dielectrics or graphene sheet itself, can supply the momentum mismatch to excite the graphene plasmons when the incident light polarized perpendicular to the grating direction. Figure 2(a) shows the simulated results of the structure shown in Fig. 1 under normal incident light, with polarization perpendicular to the ULDGs (that is, $\varphi = 0^\circ$ and $\theta = 0^\circ$). Two plasmonic resonances corresponding to the absorption peaks at 5.08 and 4.35 μm are clearly visible, which is dominant for absorptions as high as 16.93% and 26.77%, respectively. This indicates that the couplings between the incident light and these two modes are very strong. Owing to the presence of negative electromagnetic parameters, such as the negative real part of the electric permittivity or the effective refractive index, which normally entail dispersion and deceleration of light, a strong transmission phase (ϕ) dispersion is observed around the transmission dips, as shown in Fig. 2(b). This is because the existence of SPs generally depends on a negative real part of the dielectric constant. Therefore, in the presence of these transparency dips, remarkable positive delay times are obtained, indicating its potential applications in slow-light devices. For example, at a resonance of 4.35 μm , where 70.55% of PIT transmission is obtained, the incident wave experiences a time delay of approximately 0.89 ps, which corresponds to a 266 μm distance delay with respect to the propagation in free space.

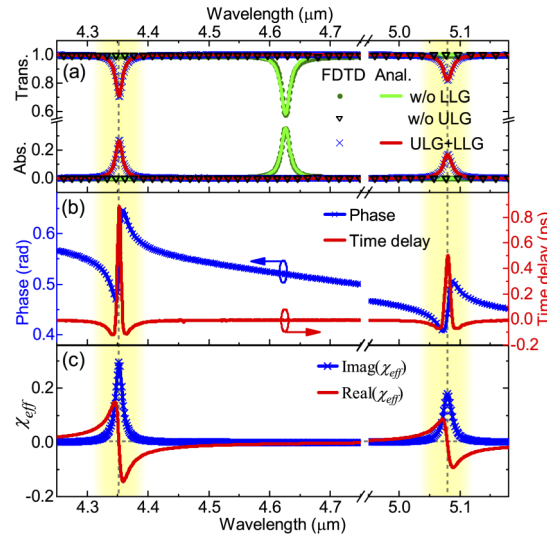


Fig. 2. (a) Transmission and absorption spectra of the system under normal incident light ($\varphi = 0^\circ$) with polarization angle $\theta = 0^\circ$. Solid curves and symbols denote the theoretical and numerical results, respectively. (b) Transmission phase (left y axis) and delay time (right y axis) of the spectrum shown in (a). (c) Real and imaginary parties of effective electric susceptibility.

To formally validate the PIT phenomenon in the coupled graphene system, we use an analytical model based on a two-particle model expressed as the following set of coupled differential equations [40,41]

$$x_1''(t) + \gamma_1 x_1'(t) + \omega_1^2 x_1(t) + \kappa_1^2 x_2(t) = Q_1 E \cos \theta / M_1 \quad (1)$$

$$x_2''(t) + \gamma_2 x_2'(t) + \omega_2^2 x_2(t) + \kappa_2^2 x_1(t) = Q_2 E \sin \theta / M_2 \quad (2)$$

Here, x_1 (x_2), γ_1 (γ_2), ω_1 (ω_2), Q_1 (Q_2), and M_1 (M_2) are the displacement vector, loss factor, resonant frequency, effective charge, and effective mass of ULG (LLG), respectively. κ_1 (κ_2) defines the coupling contribution of the directly excited plasmons (in the frequency domain), which couple from the LLG (ULG) graphene layer to the ULG (LLG). In the above differential equations, the terms on the right-hand side can be considered as the directly excitation efficiency of the resonators. Then, by substituting $Q_2 = Q_2/A$ and $M_2 = M_2/B$, where A and B are dimensionless constants referring to the relative coupling of the resonating modes in the graphene payers with the incident electromagnetic wave $E = E_0 e^{i\omega t}$, and assuming the displacements vectors for upper and lower graphene as $x_1 = c_1 e^{i\omega t}$ and $x_2 = c_2 e^{i\omega t}$, we can solve the above coupled equations as:

$$x_1(t) = \frac{[B\kappa_1^2 \sin \theta / A + (\omega^2 - \omega_2^2 - i\omega\gamma_2) \cos \theta]}{\kappa_1^2 \kappa_2^2 - (\omega^2 - \omega_1^2 - i\omega\gamma_1)(\omega^2 - \omega_2^2 - i\omega\gamma_2)} \frac{Q_1}{M_1} E \quad (3)$$

$$x_2(t) = \frac{[\kappa_2^2 \cos \theta + B(\omega^2 - \omega_1^2 - i\omega\gamma_1) \sin \theta / A]}{\kappa_1^2 \kappa_2^2 - (\omega^2 - \omega_1^2 - i\omega\gamma_1)(\omega^2 - \omega_2^2 - i\omega\gamma_2)} \frac{Q_1}{M_1} E \quad (4)$$

The effective electric susceptibility (χ_{eff}), which corresponds to the ratio of the polarizability (P) of the particle to the amplitude of the incident electric field (E), can then be written in terms of the displacement vectors as:

$$\begin{aligned} \chi_{eff} &= \frac{P}{\epsilon_0 E} = \frac{Q_1 x_1 + Q_2 x_2}{\epsilon_0 E} \\ &= \frac{K}{A^2} \left[\frac{A(B\kappa_1^2 \sin \theta + \kappa_2^2 \cos \theta)}{\kappa_1^2 \kappa_2^2 - (\omega^2 - \omega_1^2 - i\omega\gamma_1)(\omega^2 - \omega_2^2 - i\omega\gamma_2)} \right. \\ &\quad \left. + \frac{B(\omega^2 - \omega_1^2 - i\omega\gamma_1) \sin \theta + A^2(\omega^2 - \omega_2^2 - i\omega\gamma_2) \cos \theta}{\kappa_1^2 \kappa_2^2 - (\omega^2 - \omega_1^2 - i\omega\gamma_1)(\omega^2 - \omega_2^2 - i\omega\gamma_2)} \right] \end{aligned} \quad (5)$$

where $K = Q_1^2 / \epsilon_0 M_1$ denotes the proportionality factor.

The simulated transmission spectra in Fig. 2(a) can be fitted by using the imaginary part of the linear susceptibility. To this end, the transmission coefficient is calculated by the Kramers–Kronig relations, which is defined as $Trans = 1 - \text{Im}[\chi_{eff}]$ [40]. This coefficient is obtained from the relation of energy conservation $Trans + Abs = 1$, where $Abs = \text{Im}[\chi_{eff}]$ is the absorption of the coupled graphene system. For the fit, the values of A and B are set to be $A = B = 1$, as the effective charge and mass of the upper and lower graphene layers are of the same geometry. This means each of the upper and lower grating-loaded graphene layers have the same potential ability to couple with the incident light. Then, we plot the analytically modeled transmission and absorption coefficients in Fig. 2(a), which agrees well with the corresponding numerical curves. Moreover, the effective susceptibility presents a clear Lorentz resonant line shape, which agrees perfectly with the excitation of the two plasmonic resonances, as shown in Fig. 2(c). Among these fittings, the excellent fittings of these curves are found for parameters $K = 5.85$ THz, $\gamma_1 = 0.19$ THz, $\gamma_2 = 0.21$ THz, $\kappa_1 = 1.86 \times 10^{-5}$ THz, and $\kappa_2 = 28.99$ THz. This suggests that, within the coupled grating-loaded system, plasmon oscillations on the ULG can strongly couple with the incident wave when it is polarized perpendicular to the gratings. Under this condition, the ULG functions in the bright mode. However, owing to a strong momentum mismatch, plasmons cannot be directly excited when the polarization is parallel to the LLG. Conversely, the LLG functions in the dark mode but can couple with the bright mode. This coupling induces the PIT effect. Note that these analyses are consistent with the numerical results plotted in Fig. 2(a).

To further evaluate the excitation of the bright and dark plasmon modes in the system, the influence of the polarization angle on the transmission curves was studied. We find that the

excitation efficiency will reach its maximum and minimum when the incident electric field is perpendicular and parallel to the gratings attached with only one layer of graphene, respectively, as shown in Figs. 3(a) and 3(b). Because each of the grating orientations is perpendicular to the other, the observations of the construction without LLG do not differ from those of the case without ULG, except for a relative 90° angular difference in polarization. This suggests that without the presentation of either of the graphene layers, only one mode can be directly excited, resulting in only one absorption peak in the spectrum. With the lack of any of the dielectric grating layer, PIT effect becomes sensitive to polarization (shown in Fig. 3(c)). This is because the graphene layer can only play the role of polarization-sensitive bright mode and polarization-insensitive dark mode with and without the gratings, respectively.

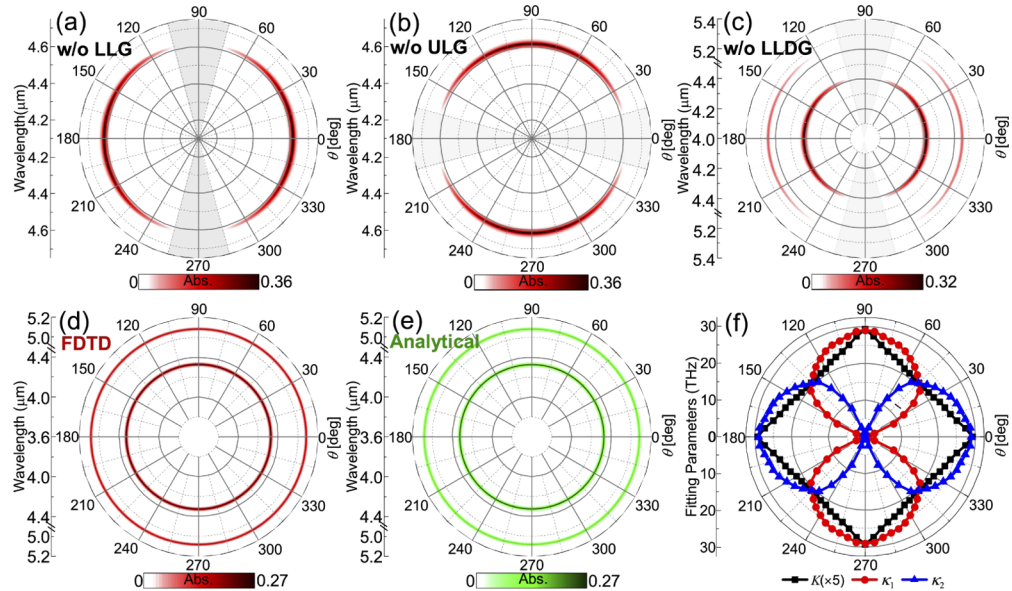


Fig. 3. Numerical (a, b, c, and d) and analytical (e) absorption maps of the situations without LLG (a), ULG (b), LLDGs (c), and with two graphene layers loaded with dielectric gratings (d and e) as functions of wavelength and polarization angle θ . (f) Fitting parameters in (e) as a function of θ .

However, with the coexistence of the two graphene layers loaded with dielectric gratings, plasmon modes can be directly excited in both the layers simultaneously or only in one individually, depending on the polarization direction. This indicates that, when the polarization is at an angle or perpendicular/parallel to the dielectric gratings, there are always two bright modes or a simultaneous bright mode and a dark mode, respectively. When the modes in the two graphene layers are brought in close proximity in both the spatial and frequency domains, they can couple and further results in a transmission window.

The physical mechanism behind this coupling behavior can be uncovered by exploring the electric field and the corresponding E_z component distributions at the two transmission dips of Fig. 2(a) for the case with $\theta = 0^\circ$, which is plotted in Figs. 4(a) and 4(d). According to the spatial distributions of the E_z components at the surface of the graphene sheets, the resonance of the mode at 5.08 μm is in-phase within the graphene layers. Thus, this plasmon mode is named the symmetric mode (SM) owing to its out-of-plane nature of the field distributions (see Appendix D). The resonance of the mode at 4.35 μm is characterized by antisymmetric charge oscillations (see Appendix D); therefore, it is named the antisymmetric mode (AM). Moreover, these plots clearly illustrate the nature of the two modes. The E_z components outline an electric dipole

mode oscillation exhibiting a 2π phase change in every period [42]. Therefore, both of these modes are the fundamental localized plasmon modes, characterized by strong field enhancement and high absorption exceeding 16%. Interestingly, it is found that the mode polarity of ULG is identical to that for the case with only ULG. However, the directly excited mode in the ULG will interface with the LLG through single coupling from the bright to the dark mode, inducing two modes in the LLG with opposite polarity distributions, as shown in Figs. 4(a) and 4(d) and demonstrated in Appendix D. Indeed, the inverse of the oscillation charges yields two separate forbidden transitions while causing an allowable transition window at the position corresponding to the original transmission dip of the situation with only ULG (see Fig. 3).

To explore the physical mechanism more thoroughly, we also display the electric field intensity profiles for the cases with 45° and 90° polarization in Fig. 4. For the case with $\theta = 90^\circ$, the field distribution opposes that in the case with $\theta = 0^\circ$. This occurs because the LLG is directly excited and further couples with the ULG at this polarization (see Appendix D). Particularly, when $\theta = 45^\circ$, both ULG and LLG can directly couple with the incident light at the same wavelength as the geometric parameters of the two layers are identical (e.g., $W_1 = W_2$, $h_1 = h_2$, and $p_1 = p_2$), as can be seen in Figs. 3(a) and 3(b). Therefore, the plasmonic oscillations can be perceived as a hybrid resonance of directly excited and induced modes, as can be seen from Fig. 4(b) for the SM and in Fig. 4(e) for the AM. In other words, at the two resonant positions, both ULG and LLG behave as bright and dark modes simultaneously at the same frequency, and the plasmonic coupling pathways are between the bright–dark and bright–bright modes simultaneously at this polarization, (see Appendix D). Excepting these three particular angles, the proposed PIT is a result of the hybridized interactions with bright to bright and bright to dark modes coupling ways when the polarization is oblique to the dielectric gratings, which is very similar to the case with $\theta = 45^\circ$, but with stronger or weaker excitation intensity of the bright modes depending on whether the polarization angle is smaller than 45° or not with respect to the corresponding gratings. Therefore, what is necessary to emphasize here is that the related coupling mechanism differs greatly from conventional PIT effects, in which the bright and dark resonators are excited only in separate resonators under one special polarization angle [24,26,28,30,31,33]. More details concerning how the bright mode is excited and further coupled with the dark mode, and how the plasmon field is resonant at the two modes can be found in the Appendix D.

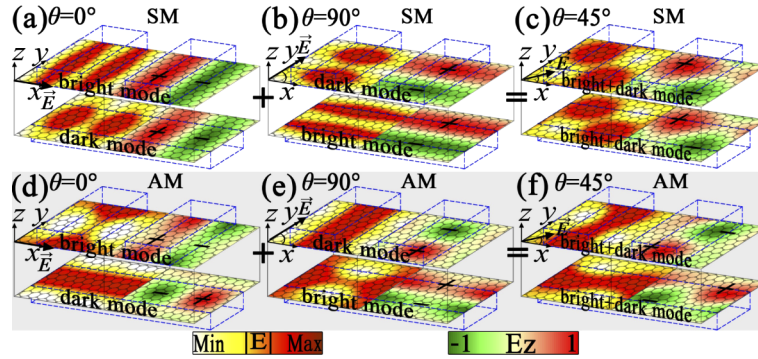


Fig. 4. Spatial distributions of the electric field (left panels) and the corresponding z component (right panels) of the SM (a)–(c) and AM (d)–(f) at polarization angles θ of 0° ((a) and (d)), 45° ((b) and (e)), and 90° ((c) and (f)). Signs “+” and “−” represent the resonating surface charges; the darker color denotes a larger charge density.

In addition to introducing bright and dark resonators, another excellent property of the proposed design is that it is totally independent of the polarization direction. Figure 3(d) reveals that the characteristic parameters of the PIT spectra, such as the absorption peaks and positions

and spectra linewidths, are completely independent of the polarization direction. To explain this, we have analytically fitted the absorption coefficient by using the imaginary part of the linear susceptibility and presented the results in Fig. 3(e). The results agree well with the related numerical results of the system, indicating that two particle model can explain well this PIT effect. Moreover, the fitting parameters are also represented for different θ in Fig. 3(f), showing that the excitation efficiency directly determines the plasmonic coupling to the other resonator, which is strongly dependent on the polarization direction. These fitting parameters can always guarantee that $\text{Im}(\partial\chi_{\text{eff}}/\partial\omega)|_{\omega_{\text{SM}}} = \text{Im}(\partial\chi_{\text{eff}}/\partial\omega)|_{\omega_{\text{AM}}} = 0$, $\text{Im}(\partial^2\chi_{\text{eff}}/\partial\omega^2)|_{\omega_{\text{SM}}} < 0$ and $\text{Im}(\partial\chi_{\text{eff}}/\partial\theta)|_{\omega_{\text{SM}}} = \text{Im}(\partial\chi_{\text{eff}}/\partial\theta)|_{\omega_{\text{AM}}} = 0$, $\text{Im}(\partial^2\chi_{\text{eff}}/\partial\omega^2)|_{\omega_{\text{AM}}} < 0$, which implies that both the resonance positions and amplitude remain the same for all polarization directions. Moreover, it is also interesting to note that other properties of this PIT effect, such as the time delay and dielectric sensitivity, are also totally insensitive to polarization (not shown here).

Because the PIT effect is caused by strong near-field couplings, parameters that strongly modulate the plasmonic response can be treated as an adjustable method to tune the transparency effect. To uncover these parameters, we performed parametric simulations for the $\theta = 0^\circ$ case by changing the widths of the two grating layers from 10 to 100 nm, and we plotted the results in Figs. 5(a) and 5(b), respectively. Considering that the ULDGs directly affects the bright mode excited on the ULG, any variation in their dimensions directly impacts the optical response of the plasmonic system. For instance, the coupling efficiency with incident light is very weak when W_1 is very small, leading to a high transparency of the layered system. While W_1 is sufficiently large, and particularly when $W_1 = 100$ nm (i.e., the ULDGs change into a whole dielectric layer), the two grating layers cannot couple with the external field and, thus, turn into dark modes because they are totally transparent, resulting in the disappearance of PIT. Notably, the system shows the best matches with the external field when W_1 is approximately 50 nm (see the dotted dark line in Fig. 5(d)). In contrast, variations of gratings width (W_2) under the dark mode graphene only allow adjustments to the resonant positions and the plasmonic losses of the SM and AM, instead of eliminating or even significantly modulating the high coupling efficiency, as can be seen in Fig. 5(e). Even when the LLDGs become an integrated dielectric layer ($W_2 = 100$ nm), the two grating layers still couple with high efficiency. In this condition, the structure turns into a two-dimensional case described in a previous study [30]. In contrast to the grating width, the change in grating height only affects the coupling efficiency while maintaining the resonant positions because it is determined by the width of the gratings only, and the maximum absorption is reached at a certain thickness (Fig. 5(g)). However, as shown in Fig. 5(h), the resonant positions exhibit a linear dependence on the refractive index of the gratings, and the absorptions approach the maximum as the refractive index increases. This indicates that gratings with higher refractive indices are more suited for coupling with the incident light.

Moreover, when we retain the grating geometry and then increase the separation distance d between the two layers, the interaction strengthens initially and then weakens (see Fig. 5(f)). Simultaneously, the resonant wavelength of the SM decreases monotonically and approaches that of the AM, while the AM decreases to the minimum when the coupling strength to the dark mode reaches the maximum, as shown in Fig. 5(c). If the distance continuously increases and is sufficiently large (for example, >100 nm), the couplings between the two grating layers are expected to be very weak as the lower grating layer is not within the decay length of the upper layer. Consequently, the SM disappears, the lower layer gratings become totally dark, and only the upper layer gratings can support the plasmon resonances, which further approaches the situation with only the ULDGs at larger distance.

Apart from geometrical structures, recent progress in nanotechnology and new findings have allowed us to achieve broad and active tunability of the optical properties of graphene through electrostatic gating techniques. This method allows to dynamically modulate the carrier concentration (thus the Fermi level) of the graphene by employing an electrolytic gate with

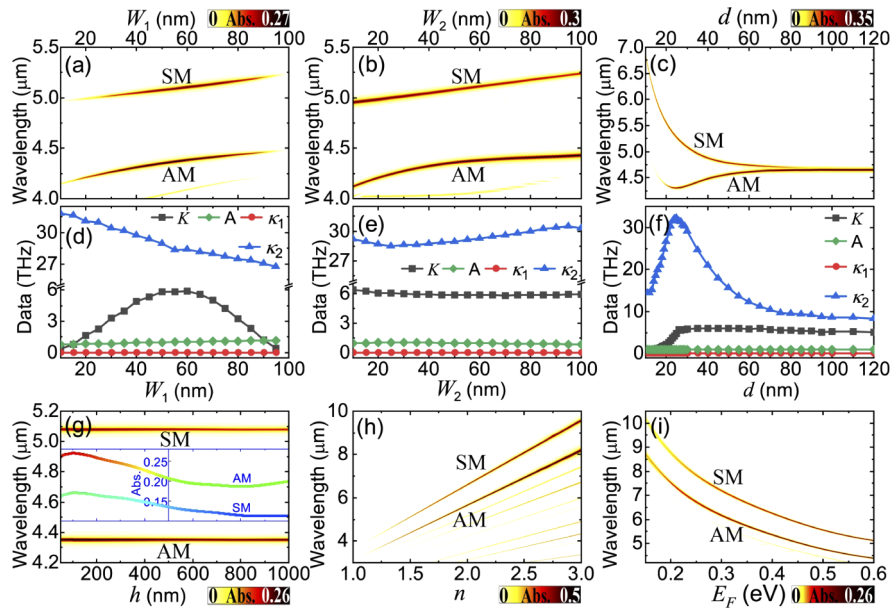


Fig. 5. 2D plot of transmission spectra of the construction with $\theta = 0^\circ$ depicting the incident wavelength as functions of (a) the grating width W_1 of ULDGs, (b) the grating width W_2 of LLDGs, (c) the separation distance d between the two graphene layers, (g) grating height, (h) refractive index of the gratings, and (i) Fermi level of the graphene sheets. (d) – (f) Fitting parameters corresponding to (a) – (c), respectively.

a field-effect transistor structure. Therefore, the position of the transmission window can be continuously tuned to a wide range of working wavelengths without re-fabricating the physical structure [43,44]. Considering that the Fermi level of graphene was reported to be experimentally feasible with a value of up to 0.8 eV [44] and even reaching 1.2 eV [45] by using this structure, herein, it is conservatively assumed that the range of Fermi energy E_F can be actively controlled between 0.1 and 0.6 eV. From a practical perspective, the proposed design depicted in Fig. 1 is feasible by designing two electrical gates on two sides of the graphene sheets so that the doping concentrations in each graphene layer can be dynamically tuned. Figure 5(i) identifies this wide-band and active plasmonic nature by altering the Fermi level; with the increase in E_F , the two plasmon modes become closer and more pronounced, and they continuously blue shift simultaneously. This figure also confirms that, when fixing the grating dimensions and interlayer distance, the resonant wavelengths of the plasmon follow a scaling rule given by $\lambda \propto (1/E_F)^{1/2}$ [46]. This relation is a universal feature of two-dimensional electron gases [43] and can benefit the design of active plasmonic devices.

3.2. Switchable double-window PIT

In the previous section, we proved that an obvious PIT window can be obtained by designing crossed dielectric grating layers on the sides of the two graphene layers. Because the geometrical parameters of the two grating layers are identical, plasmons are generated at the same position on the two graphene layers. Owing to the equivalent and complementary coupling between the two graphene layers, the induced transparency window is totally insensitive to polarization. Therefore, the transmission line always maintains the same appearance in any polarization direction. However, the transparency window can be induced by either single coupling from bright to dark mode for the case when the electric direction of the incident light is polarized

perpendicularly or parallelly to the gratings, or hybridized bidirectional coupling from bright to bright and bright to dark modes, when the incident light is polarized at an angle with respect to the gratings. It is known that the geometric symmetry of a system plays a fundamental role in affecting its optical properties. This also applies for plasmonic systems where the near-field coupled optical phenomena such as PIT require strong optical interactions between symmetric-broken resonators. In this section, we demonstrate this point by using inhomogeneous gratings with different widths and refractive indices, where different resonant positions in the two grating layers will induce double-window PIT effects.

Figure 6(a) shows the absorption map as functions of the incident wavelength and polarization angle θ for $W_1 = 30$ nm and $W_2 = 70$ nm. This figure clearly indicates that, in contrast to the case with uniform gratings (as can be seen in Fig. 3(d)), the absorption is highly sensitive to the polarization direction. For a better understanding of this response, we selected three particular absorption spectra for the cases with $\theta = 0^\circ$, 45° , and 90° ; they are displayed in Fig. 6(b). For the case with $\theta = 0^\circ$ or 90° , two absorption peaks along with one transmission window are observed. Particularly, when the incident light is polarized inclinedly to the gratings, four absorption peaks and two induced transmission windows, which are at the resonant positions of the two original systems without ULG and LLG, are observed. Similarly, for the situation with different dielectric indices in the gratings, e. g., $n_1 = 2.0$, $n_2 = n_3 = 2.5$, the unequal couplings between the two graphene layers will result in highly polarization-dependent absorptions, as shown in Figs. 6(c) and 6(d). The physical mechanism can be ruled out as a cause for the polarization-dependent single- and double-window PIT effects by investigating the modes excited in individual graphene layers. Firstly, as for the polarization insensitive single window PIT, because of the particular geometrical arrangement of the two grating layers, the size-dependent plasmonic resonances are excited at the same position. With the variation in polarization direction, irrespective of the strengthening or weakening of the excitation efficiency of the bright or dark mode in one graphene layer, it will be compensated for by the other graphene layer, inducing the insensitivity of the system towards the polarization direction. That is, each graphene layer can behave as a bright or dark mode individually, or both bright and dark modes simultaneously, depending on the polarization direction. For the situation with unequal grating widths and refractive indices, the directly excited bright mode and induced dark modes on the two graphene layers will be generated at different wavelengths, which will result in incoordinate interactions and further lead to the polarization-dependent PIT effects with different transparency windows. Because the directly excited plasmonic resonances are at different positions, the corresponding PIT effects are the result of single coupling from bright to dark mode. Therefore, the two PIT windows arise from two bright-dark mode coupling pathways.

3.3. PIT with other grating types

In the previous sections, we have explained in detail that graphene layers attached with crossed rectangular gratings can couple to induce polarization-independent or polarization-dependent transparency window. In fact, this design method is entirely applicable to any type of grating—rectangular [46], trapezoidal [47], sinusoidal [48,49] and other shaped [50] surfaces or specially doped dielectric configurations [51], or gratings composed of specially doped graphene conductivity [52], sinusoidally shaped graphene sheet itself [53], or patterned graphene nanoribbons—[32] provided the gratings can supply the momentum mismatch for incident radiation to excite the graphene plasmons in one direction when presented alone. In this section, this general concept is confirmed by three typical gratings formed by dielectrics with sinusoidally shaped surfaces (Fig. 7(a)), specially doped configurations (Fig. 7(e)), and graphene sheet itself with specially doped conductivity (Fig. 7(i)). To investigate how these gratings excite and affect the plasmonic couplings of the graphene layers, we performed first-principles electromagnetic simulations using a finite element method (FEM) solver, COMSOL, for the structures. Further

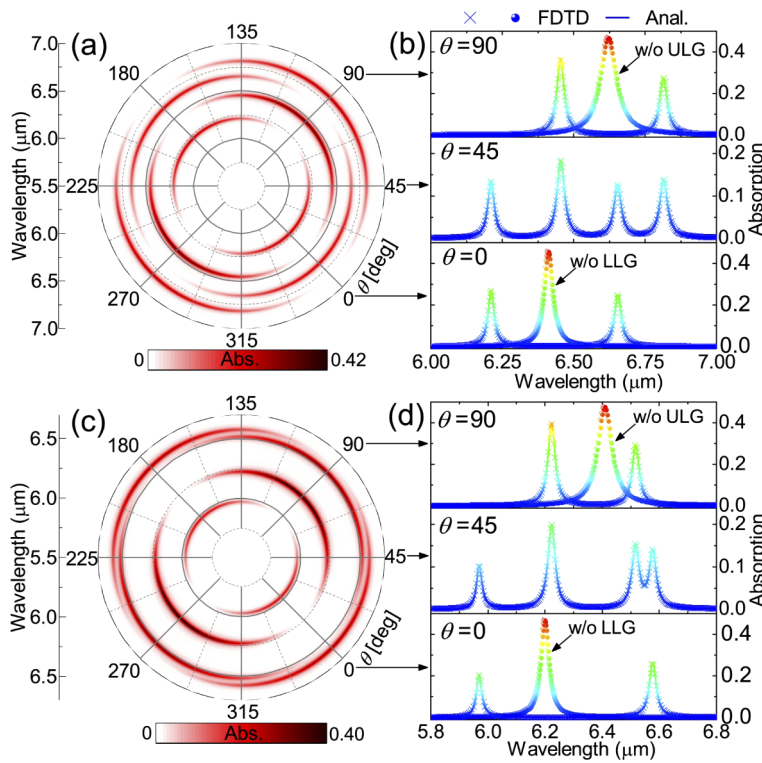


Fig. 6. Absorption maps of the asymmetrical PIT structure (a) with $W_1 = 30 \text{ nm}$ and $W_2 = 70 \text{ nm}$ and (c) with $n_1 = 2.0$, $n_2 = n_3 = 2.5$ plotted as functions of wavelength and polarization angle θ , respectively. (b) and (d) Absorption spectra of the system corresponding to (a) and (c) for polarization angles of 0° , 45° , and 90° , respectively. The solid curves are the results from the analytical model, and the symbols are from the numerical simulations. Other parameters can be found in the Appendix C: Table 1.

details regarding the geometric parameters and numerical simulations can be found in the Appendixes B and C. As shown in Figs. 7(b), 7(f) and 7(j), the designed two crossed grating layers result in one transparency window in the spectrum. It is found that not only the transmission spectra are totally polarization-independent (Figs. 7(c), 7(g) and 7(k)), but also the corresponding time delays and refractive sensitivities (Figs. 7(d), 7(h) and 7(l)). Those PIT phenomena can be well explained by investigating the coupling mechanism, which can be understood by considering the bright–dark and bright–bright coupling pathways, as the results match well with that of the two-particle model. As expected, without the lower layer grating, the induced PIT effects are no longer observed. Moreover, the polarization-dependent double-window PIT effects can be induced when the two grating layers are designed with different parameters (not shown here).

3.4. PIT in in-plane anisotropic 2D materials

With the emergence of graphene, a class of atomically thin 2D materials, such as group V mono- and multilayers, the 1T phase of the transition metal dichalcogenides [54,55], trichalcogenides [56], and, most notably, black phosphorus (BP) [57,58], have also received a burgeoning amount of attention in recent years owing to their exciting in-plane anisotropic electronic and optical properties. In these media, the permittivities are anisotropic because their effective masses are different along the two principal crystal directions, which can fundamentally alter how light interacts with matter [13]. Indeed, at zero temperature and in the absence of doping, these 2D

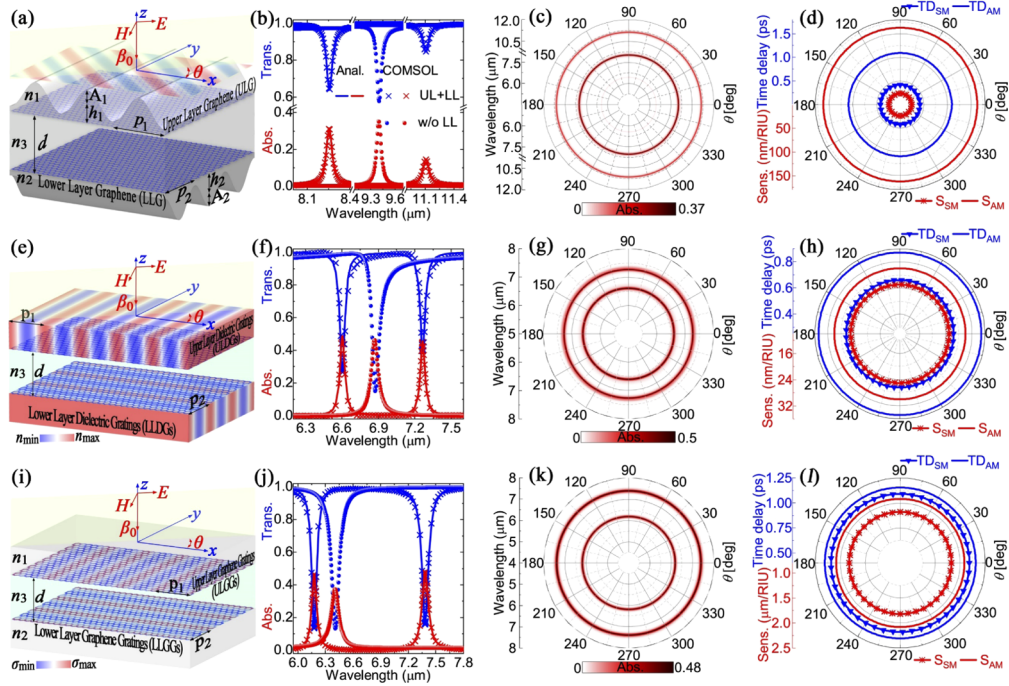


Fig. 7. Schematic of the PIT system with gratings formed by sinusoidal dielectric surfaces (a), periodic dielectric refractive index (e), and periodically doped graphene conductivity (i). Two graphene layers are sandwiched between the two grating layers with crossed directions separated by a conductor with index n_3 and thickness d . A linearly polarized plane wave with wave vector β_0 and polarization angle θ with respect to the x axis impinges on the constructed graphene-layered system. (b, f, and j) Transmission and absorption spectra for the case with $\theta = 0^\circ$. Solid curves and symbols represent the theoretical and simulated results, respectively. (c, g, and k) Absorption maps of the designs as functions of the wavelength and polarization angle θ . (d, h, and l) Time delays (blue lines) and refractive index sensitivities (red lines) for different θ . Details of the parametric settings can be seen in the Appendix C: Table 2.

sheets do not support plasmons. However, theoretical and experimental studies have confirmed that excitations on these sheets can be activated by introducing additional doping charge carriers [12], offering a new class of platforms to achieve novel anisotropic photonic properties in ultracompact form factor. Among them, monolayer BP has been extensively studied as a highly anisotropic and dynamically tunable plasmonic material [13,57]. In contrast to the isotropic 2D plasmonic materials, its inherent in-plane anisotropy renders the plasmon resonance dependent on the direction [8]. Based on this, without loss of generality, we focus on BP to demonstrate the mechanism by which fully polarization-insensitive PIT can be achieved in anisotropic 2D materials.

The proposed design is similar to the isotropic case, as shown by Fig. 8(a). Because BP has two principal lattice axes, that is, “zigzag” (ZZ) and “armchair” (AC), there are three configurations for the two stacked BP monolayers: (i) with ZZ lattice aligned along the x direction in the two layers (that is with ZZ lattice grating in the upper layer and AC lattice grating in the lower layer), (ii) with ZZ lattice aligned along the x direction in the upper layer and AC lattice aligned along the x direction in the lower layer (that is with ZZ grating in the two layers), and (iii) with AC lattice aligned along the x direction in the upper layer and ZZ lattice aligned along the x

direction in the lower layer (that is with AC grating in the two layers). To investigate the effect of anisotropic optical properties on the PIT behavior of BP, the structural parameters for both ZZ and AC directions in the two grating layers are chosen to be the same for all the applied configurations. We perform FDTD simulations for the three different configurations. More details on the dielectric constants, geometric parameters, and optical conductivity of BP can be found in the Appendixes A and C. Here, we emphasize that, although isotropic materials such as graphene also have ZZ and AC boundaries, our classical analyses have neglected any effects that may arise from the possible quantum finite-size effects and the termination effects from atomic edges, because the minimum widths of the considered dimensions are much wider than 10 nm [37,59]. Instead, we used the two edge types only to distinguish the crystallographic orientation-dependent anisotropic directions. Moreover, in this study we only focus on the pure anisotropic dielectric situation with $\text{Im}[\sigma_{BP,xx} \cdot \sigma_{BP,yy}] > 0$, excluding the hyperbolic situation (that is $\text{Im}[\sigma_{BP,xx} \cdot \sigma_{BP,yy}] < 0$). More detailed research on hyperbolic plasmons in BP can be found in previous studies [8,60].

Now we investigate the PIT effects in the three configurations. The first one is with ZZ grating in the upper layer and AC grating in the lower layer. In this configuration, when the incident beam is polarized along the x direction ($\theta = 0^\circ$), localized plasmon resonance in the upper ZZ grating can be directly excited while the lower AC grating cannot. The excited mode will further couple with the lower layer grating, resulting in two absorption resonance peaks corresponding to symmetric and antisymmetric field distributions in the spectrum, as shown in the Fig. 8(c) and Appendix E. Under this condition, the upper layer BP (ULBP) plays the role of the bright mode, while the lower layer acts as the dark mode. This one-way bright–dark mode coupling directly leads to the PIT window in the spectrum. However, without the presentation of lower layer BP (LLBP), only the dipole mode in the upper layer ZZ grating is excited at the position between that of the two coupled modes in the two BP layers. When light is polarized along the y direction ($\theta = 90^\circ$), localized plasmon resonance in AC grating in the lower layer can be directly excited while that in the upper ZZ grating cannot. However, the latter can couple with the upper layer grating. Thus, we observe two absorption resonance peaks in the spectrum. In this polarization, the LLBP works as the bright mode, and the upper layer as the dark mode. As shown in Fig. 8(c), when compared with x polarization (bright ZZ grating in upper layer), the resonances for y polarization (bright AC grating in lower layer) shift to shorter wavelengths owing to the smaller effective mass along the AC direction [57], as expected from Eqs. (1)–(5). Interestingly, for a polarization angle of 45° , plasmon resonances in the ZZ and AC directions can be excited simultaneously. Because of the anisotropic optical properties of BP, the resonant wavelengths are different but are in the same positions that respectively correspond to the x and y polarizations. The directly excited plasmons in each BP layer will couple with the other layer. This further leads to two separate groups of symmetric and antisymmetric modes, resulting in four absorption peaks. Those absorption peaks indicate that, in this polarization, the upper- and lower-layer BPs play the role of both bright and dark modes simultaneously at different resonant wavelengths. It is their two-way bright–dark mode couplings that led to two transmission windows in the spectrum. Note that this double-window PIT effect is absolutely because of the anisotropic optical properties of BP instead of the geometrical asymmetry in the case with isotropic graphene (as shown in Fig. 6). The anisotropic properties of BP will lead to polarization-dependent single- or double-window PIT effect, as depicted in Fig. 8(b). Further details about the electric field intensity and distributions at the resonant wavelengths can be found in the Appendix E.

For the second case, both the grating layers are constructed with ZZ grating. In this condition, except for the orientation angle difference of 90° , all the related plasmonic parameters in the two grating layers, including geometrical dimensions and dielectric constants (like effective mass and lattice orientation) along the grating directions are the same. That is, according to Eqs. (1) and (2), the plasmonic response is the same as the isotropic situation. Therefore, the case without LLBP

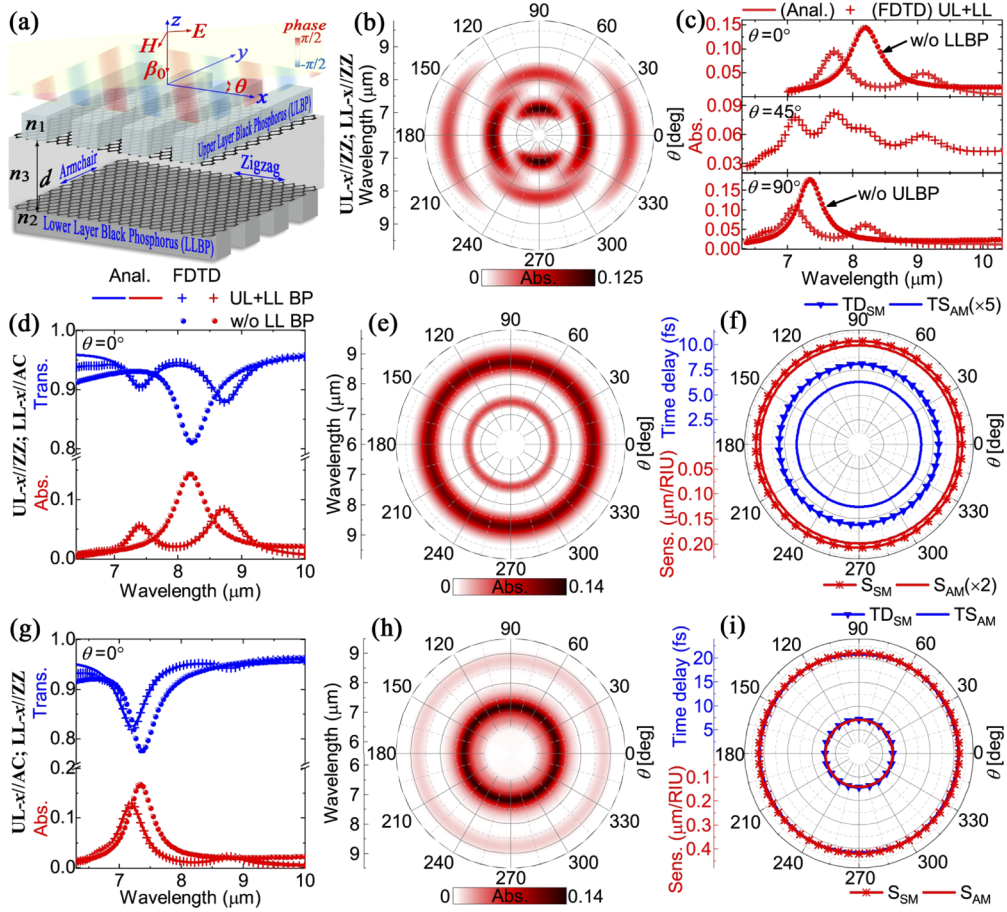


Fig. 8. (a) Schematic of the PIT system with two black phosphorus layers sandwiched between two periodic dielectric gratings with crossed directions in the x - y plane, and separated by a Si or SiO_2 conductor with refractive index n_3 and thickness d . (b, e, h) Absorption maps of the design as functions of the wavelength and polarization angle θ . (c, d, g) Transmission and absorption spectra for some particular polarization angles. Solid curves and symbols represent the analytical and numerical results, respectively. (f) and (i) Time delays (blue lines) and refractive index sensitivities (red lines) for different polarization angles θ . The cases with different BPs along both the ZZ and the AC directions are shown. (b) and (c) are for the situation with zigzag (ZZ) lattice in the x directions in the two BP layers, (d-f) correspond to the situation with ZZ lattice in ULBP and armchair (AC) lattice in the LLBP in the x direction, while (g-i) are for the case with AC lattice in ULBP and ZZ lattice in the LLBP in the x direction, respectively. Detailed parametric settings can be found in the Appendix C: Table 1.

is the same as that without ULBP, except for difference of 90° in polarization direction. With the coexistence of the two BP grating layers, identical plasmon modes can be directly excited in the two BP layers simultaneously or only in one BP layer individually, depending on the polarization direction. This indicates that there are always two bright modes or a bright and a dark mode simultaneously, when the polarization is at an angle with or perpendicular/parallel to the dielectric gratings, respectively. When the modes in the two BP layers are close enough, a transmission window is observed, owing to either one-way bright-dark or bidirectional bright-bright and

bright–dark modes hybridized couplings, as illustrated in Figs. 8(d) and 8(e). Most importantly, one excellent feature of this PIT effect is its inertness to the polarization direction. A transmission map in Fig. 8(e) reveals that the characteristics of the PIT spectra, including the absorption peaks and positions, and spectral linewidths, are totally insensitive to the polarization angle. Moreover, other characteristics of this PIT effect, such as the time delay and dielectric sensitivity, are also totally insensitive to polarization (see Fig. 8(f)). The physical mechanism behind these polarization-insensitive properties can be understood in the manner as in the case of isotropic graphene, which has been explained earlier.

Finally, for the third case, both the grating layers are designed with AC grating. In this grating configuration, polarization insensitive PIT effect is observed, as illustrated in Figs. 8(g)–8(i). Except for the excitation efficiency and resonance positions, the physical mechanisms and related PIT characteristics are very similar to the second case. We have analytically fitted the absorption coefficient for the three cases using the two-particle model and have shown the results in Fig. 8. The results are in good agreement with the corresponding numerically simulated curves, indicating that two particle model can explain the PIT effects well in both the isotropic and anisotropic cases.

Apart from rectangular dielectric gratings, we also briefly discuss the gratings formed by BP nanoribbons (BPNRs) in the Appendix E as another proof-of-concept demonstration. The results were remarkably similar to those of the BP sheets: for the case with ZZ nanoribbons in the upper layer and AC nanoribbons in the lower layer, the PIT effect is polarization-dependent with single or double window. While in the cases with ZZ or AC nanoribbons in the two layers, the PIT effects are polarization-independent with single window. Based on the trends observed with rectangular dielectric BP gratings and BPNRs, and further comparing them with isotropic graphene, our treatment to achieve totally polarization-independent PIT is plausible and comprehensive. This treatment can be conservatively expanded to any type of crossed grating layers formed by either shaped dielectrics (such as periodically dope, or rectangularly or sinusoidally shaped dielectric) or the 2D crystals itself encompassing both the in-plane isotropic sheets, with any lattice orientation and anisotropic monolayer with crossed lattice directions (like periodically doped conductivity or nanoribbon gratings).

4. Conclusion

In this study, both advanced simulations and theoretical analyses were combined to investigate the PIT effects in in-plane isotropic and anisotropic 2D materials, by designing two crossed grating layers formed either by shaped dielectrics (such as rectangularly or sinusoidally shaped, or periodically doped dielectrics) or conductive 2D crystals themselves (such as periodically doped conductivity or nanoribbon gratings). With isotropic graphene and anisotropic BP as examples, we demonstrate that each grating layer can act as either the bright mode or dark mode alone, or both the bright and dark modes simultaneously, when the incident light is polarized perpendicularly/parallelly or inclinedly to the gratings, respectively. Specifically, when two isotropic (anisotropic) layers are designed with the same grating parameters (crossed lattice directions), the equivalent plasmon excitation efficiency and complemental interlayer couplings produce a single-window PIT effect with fully polarization-insensitive characteristics, while the asymmetric gratings (same lattice directions) with asymmetric plasmon excitations and interlayer interactions result in highly polarization-sensitive single- or double-window PIT. Finally, the proposed concepts were analyzed using a two-particle model, and the results showed outstanding agreement with the numerical results for all cases. Although this study is focused on isotropic graphene and anisotropic BP, its results can be completely generalized for any plasmon-supporting in-plane isotropic and anisotropic 2D materials. The developed methods provide a general approach to achieving PIT with any type of grating, encompassing both the in-plane isotropic

and anisotropic 2D materials, which can advance the practical applications of 2D material-based plasmonic devices.

Appendices

A. Dynamic permittivity and conductivity of 2D material

In our numerical simulations and theoretical analyses, the 2D material film is modeled by random-phase approximation (RPA) [61]. Within this approximation, the in-plane optical conductivity, σ , of a doped 2D material can be approximately written as a semiclassical Drude-like expression in the form of a tensor in the spectral range of interest [8,46,57]:

$$\sigma = \begin{bmatrix} \sigma_{xx} & \sigma_{xy} \\ \sigma_{yx} & \sigma_{zz} \end{bmatrix}. \quad (6)$$

Since only the in-plane isotropic and anisotropic cases instead of hyperbolic and gapped Dirac cases are considered, we have $\sigma_{xy} = \sigma_{yx} = 0$ and $\text{Im}[\sigma_{xx}\cdot\sigma_{yy}] > 0$ [8]. Considering its single-atom thickness, the permittivity of the monolayer 2D material is modeled by an anisotropic dielectric tensor. Its surface normal component is set to ϵ_{zz} , and the in-plane components are [8,46,57]:

$$\epsilon_{jj} = \epsilon_r + i\sigma_{jj}(\omega) / (\epsilon_0\omega t), \quad (7)$$

where $j = x$ and y , ϵ_r is the background permittivity, ϵ_0 is the vacuum permittivity, ω is the angular frequency of the incident beam, and t is the thickness ($= 1$ nm). The value of t is plausible owing to the large difference between the thickness of the 2D material and the size of the intervals. The simulated results show excellent agreement for $t = 0.34, 0.5$, and 1 nm, as long as the mesh is sufficiently fine.

For the isotropic case, we take graphene as an example, and we set its surface-normal component and background permittivity as $\epsilon_{g,r} = \epsilon_{g,zz} = 2.5$ based on the dielectric constant of graphite. Its optical conductivity, σ_g , in the Drude-like expression is $\sigma_{g,xx}(\omega) = \sigma_{g,yy}(\omega) = ie^2 E_F / [\pi \hbar^2 (\omega + i\tau_g^{-1})]$ [46,62]. Here, $E_F = \hbar v_F (n_g \pi)^{1/2}$ is the chemical potential of graphene, which is determined by the carrier concentration thorough $n_g = (\mu/\hbar v_F)^2/\pi$ (where $\mu = 15,000$ cm²/(V·s) is the measured dc mobility, \hbar is the reduced Planck constant, and $v_F = 10^6$ m/s is the Fermi velocity), which can be dynamically tuned by electrical gating techniques [31,43,62]. τ_g is the carrier relaxation time, which is calculated by $\tau_g = \mu E_F / (e v_F^2)$. We fix E_F at 0.6 eV, which is a relatively conservative value compared with the state-of-the-art experimentally feasible ones, unless specified otherwise (≥ 0.8 eV) [44,45].

For the anisotropic case, we focus on monolayer black phosphorus (BP). The photonic conductivity of a monolayer BP in the mid-infrared range can be described by employing a simple semi-classical Drude model, given as [13,57]

$$\sigma_{BP,jj}(\omega) = \frac{iD_j}{\pi(\omega + i\tau_{BP}/\hbar)}, \quad D_j = \pi e^2 \frac{n_{BP}}{m_j}, \quad (8)$$

where D_j is the Drude weight, $\tau_{BP} = 10$ meV is the relaxation rate, n_{BP} is the electron doping, which is chosen as 10^{14} cm⁻², and m_j is the effective electron mass near the Γ point within the Hamiltonian model, which is

$$m_x = \frac{\hbar^2}{2\gamma^2/\Delta + \eta_c}, \quad m_y = \frac{\hbar^2}{2\nu_c}. \quad (9)$$

Here, for monolayer BP, the parameters in Eq. (9) can be set as $\gamma = 4\pi/a$ eVm, with $a = 0.233$ is the scale-length of the BP, and π/a is the width of the Brillouin zone, $\eta_c = \hbar^2/(0.4m_0)$, $\nu_c = \hbar^2/(0.7m_0)$, and the band gap $\Delta = 2$ eV for a standard electron rest mass, $m_0 = 9.10938 \times 10^{-31}$ kg. At this point, the relative permittivity of monolayer BP can be calculated using Eq. (7), with a given $\epsilon_{BP,r} = \epsilon_{BP,zz} = 5.76$.

B. Numerical simulations

In the main text as well as the Appendixes, except for Fig. 7, all the other numerical results are simulated via the finite-difference time-domain (FDTD) method using Lumerical FDTD solutions. In these simulations, we impose periodic boundary conditions along both the x and y axes, and apply perfectly matched layers on the top and bottom of the unit cell to absorb the entire quantity of light approaching the boundaries. Broadband plane waves are incident from the z direction with a polarization angle θ with respect to the x axis and an incident angle φ with respect to the z axis. Since only the normally incident situation is considered, we set $\varphi = 0^\circ$ throughout the simulated models. The transmission through the system is monitored with a frequency domain monitor positioned at the far side of the substrate, while the reflection is displayed on a monitor behind the source. Electrical field distribution is gathered by 2D field profile monitors at the resonant wavelengths, which are situated at the planes 0.5 nm distance below and above the upper and lower 2D material monolayers, respectively. Moreover, in these two planes, two point-type field time monitors are placed at their respective positions where the maximum field resonance takes place, to probe the resonant field. In order to achieve convergence, the mesh element size in the vicinity of graphene is set to be much smaller than both the plasmon wavelength and the grating parameters. The mesh size inside the graphene layer is set to 0.25 nm along the z axis and 2 nm along the x and y axes, and the mesh size gradually increases outside the graphene layer. To ensure the validity of the simulation, a minimum simulation time of 10,000 fs, minimum auto shutoff value of 10^{-9} , and highest mesh accuracy are set in the model. All of the results presented in this work have been verified for convergence with respect to mesh and domain size.

While data of Fig. 7 were numerically simulated through rigorous full-wave simulations on COMSOL Multiphysics in the frequency domain using a radio frequency module. In these simulations, we used two ports placed inside the simulation domain along the z direction to introduce a plane wave with a polarization angle θ with respect to the x axis, to solve and excite the plasmon modes, and further measured the transmission and reflection spectra from the terminal interfaces. The absorption of the PIT system is given by $Abs = 1 - Trans - Ref$, where $Trans$ is the transmission, defined as $|S21|^2$, and Ref is the reflection, defined as $|S11|^2$. Perfectly matched layers were used outside of the ports to improve the efficiency and increase accuracy, while applying periodic conditions to the x and y boundaries to simulate an infinite period. The minimum mesh sizes are 4 nm in air and dielectrics and 0.5 nm inside graphene, respectively, which are much smaller than the wavelengths of incident and outgoing light ($<\lambda/1,000$, where λ is the wavelength of the free space). The mesh size near graphene is further refined to be in the range of 0.5–4 nm. We present several numerical examples to verify the accuracy of the proposed model, so that all the calculations reached proper convergence.

C. Parametric settings

Table 1. Geometrical parameters of Figs. 1, 6, 8, and 10.

Images	w_1 (nm)	w_2 (nm)	p_1 (nm)	p_2 (nm)	h_1 (nm)	h_2 (nm)	d (nm)	n_1	n_2	n_3
Fig. 1	50	50	100	100	100	100	30	1.5	1.5	1.5
Fig. 6(a)	30	70	100	100	100	100	25	1.5	1.5	1.5
Fig. 6(c)	50	50	100	100	100	100	25	2.0	2.5	2.5
Fig. 8	50	50	100	100	100	100	30	3.0	3.0	3.0
Fig. 10	50	50	100	100	\	\	30	1.0	1.5	1.0

In this section, we provide details about the parametric settings in the main text as well as in this supporting material. Table 1 shows the geometrical parameters for Figs. 1, 6, 8, and SM4. The geometrical dimensions can be found in the corresponding figures. Besides, we also list

Table 2. Geometrical parameters of Fig. 7.^a

Images	$f(i)$	f_0	a_0	a_1	p_i	φ_0	d	n_1	n_2	n_3
Fig. 7(a)	$z(i)$	1	± 35 nm	± 25 nm	100 nm	$\pi/2$	30 nm	3.0	3.0	3.0
Fig. 7(e)	$n(i)$	2	1	-0.9	100 nm	$-\pi/2$	30 nm	\	\	1.5
Fig. 7(i)	$\sigma_g(i)$	σ_g	1	-0.8	100 nm	$\pi/2$	20 nm	1.0	1.0	1.5

^aNote: The subscripts “+” and “-” denote the upper and lower layers, respectively.

the geometrical settings of Fig. 7 in Table 2. In this figure, the gratings can be described by the function $f(i) = f_0[a_0 + a_1 \sin(2\pi i p_i + \varphi_0)]$, where $i = 1$ or 2 , which correspond to the gratings in the x and y directions in the upper and lower layers, respectively. Throughout the main text as well as in this supporting material, we assume that the related parameters are the same, unless specified otherwise. We also emphasize that the results are general, and the fundamental conclusions do not depend on the particular choice of parameters for the 2D materials and the geometrical dimensions of the structure

D. Field symmetry analysis

In Fig. 4 of the main text, we determined the field symmetry in the frequency domain, which contains both symmetric and antisymmetric field distributions at the plasmon resonances. In this section, in addition to Fig. 4, we demonstrate the field symmetry at the time domain. As shown in Fig. 9, for the situation with $\theta = 0^\circ$, the upper layer graphene (ULG) can be directly excited by the incident light, so that it would work as the bright mode, while the lower layer graphene (LLG) would function as the dark mode since plasmons cannot be generated directly. Therefore, as can be seen from Figs. 9(a) and 9(d), the plasmon field is firstly generated in the ULG, which will couple with the LLG, and the LLG further couples back with the ULG. This results in the steadily symmetric and antisymmetric field distributions in the two layers. On the contrary, for the situation with $\theta = 90^\circ$, the plasmons in the LLG will be firstly excited and further couple with the ULG, as can be seen from Figs. 9(c) and 9(f). While for the case with $\theta = 45^\circ$, both ULG

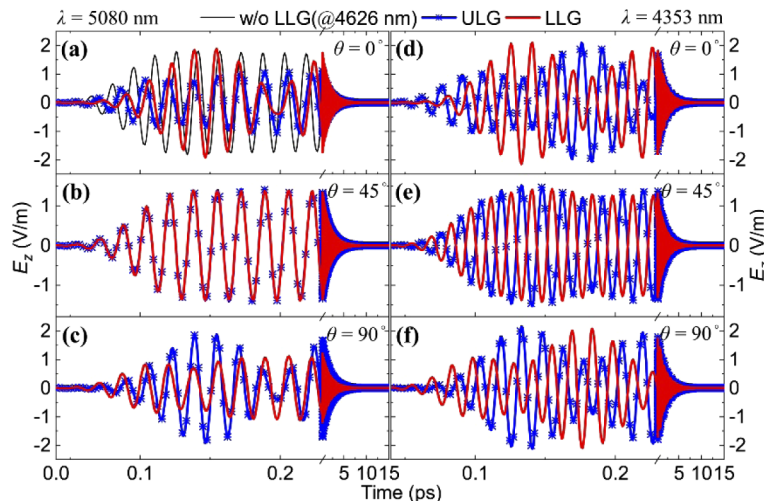


Fig. 9. Electric field resonances as a function of time of the SM at a wavelength of 5,080 nm (a-c) and AM at the wavelength of 4,353 nm (d-f) at polarization angles θ of 0° ((a) and (d)), 45° ((b) and (e)), and 90° ((c) and (f)), respectively.

and LLG can directly couple with the incident light simultaneously, and the excited plasmon modes in the two layers will interact with each other. This will further result in the in-phase and out-of-phase resonances.

E. PIT in black phosphorus nanoribbons

In the main text, we discussed the PIT effect in two BP monolayers. In this section, to demonstrate the veracity of our proposal further, we present the case with gratings formed by crossed black phosphorus nanoribbons (BPNRs). As plotted in Fig. 10, due to the difference along the two principal lattice axes of BP, the grating layers constructed by BPNRs can be divided into three cases, similar to the situation with two BP monolayers.

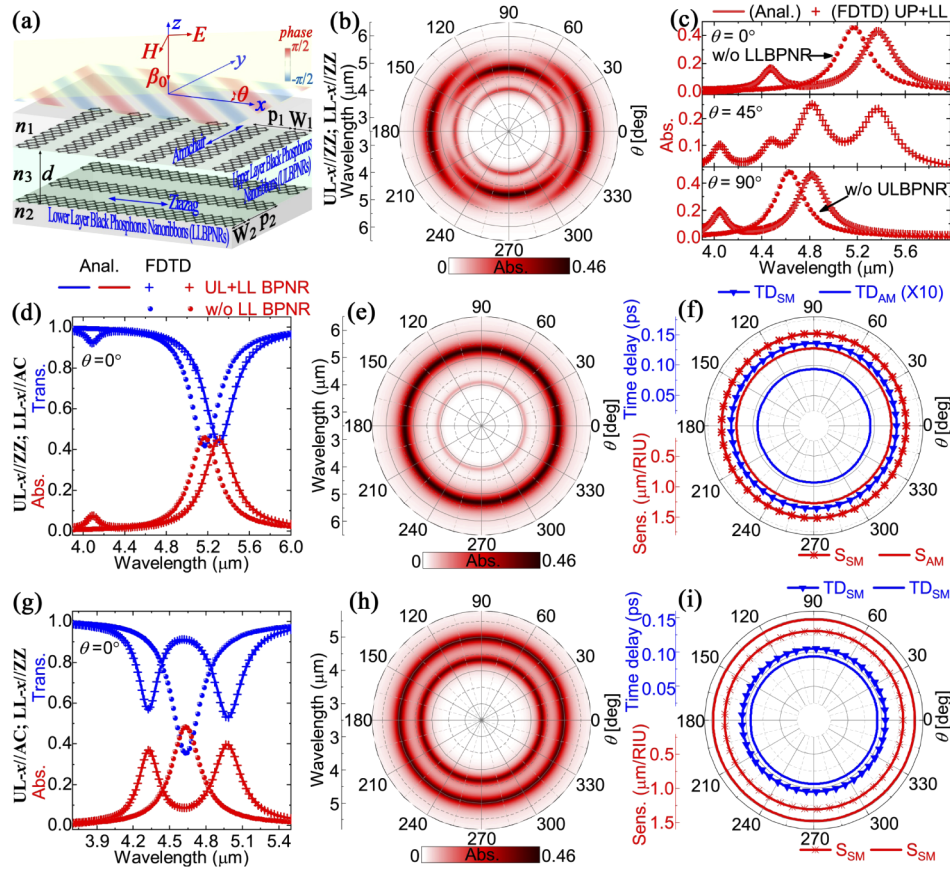


Fig. 10. (a) Schematic of the PIT system with two grating layers composed of periodic black phosphorus nanoribbons with crossed directions in the x - y plane. (b, e, h) Absorption maps of the design as functions of wavelength and polarization angle θ . (c, d, g) Transmission and absorption spectra for specific polarization angles. Solid curves and symbols represent the analytical and numerical results, respectively. (f) and (i) Time delays (blue lines) and refractive index sensitivities (red lines) as a function of polarization angle, θ . The cases of BPNRs patterned along both the ZZ and AC directions are shown. (b) and (c) are for the situation with ZZ edges in the x direction of the two BP layers, (d-f) are for the case with ZZ edge in ULBP and AC edge in the LLBP in the x direction, while (g-i) correspond to the case with AC edge in ULBP and ZZ edge in the LLBP in the x direction, respectively. Detailed parametric settings can be found in this Appendix C: Table 1.

The first case is configured with ZZ lattice axes along the x direction in the two layers (that is, with AC ribbon edge in the upper layer and ZZ ribbon edge in the lower layer, which, for the convenience of discussion, are respectively called ZZ and AC gratings since the grating period is parallel to these lattice directions), as shown in Fig. 10(a). In this case, the crystallographic orientations of atomic edges are different in the two BPNR layers; therefore, the directly excited localized plasmons on them will be different. To elaborate, when the incident light is polarized along the x direction ($\theta = 0^\circ$), localized plasmon resonance in the upper layer BPNRs (ULBPNRs) can be directly excited, so they will work as the bright mode. The lower layer BPNRs (LLBPNRs) cannot directly couple with the incident light; thus, they will play the role of the dark mode. It is the one-way bright–dark mode interactions that directly lead to the PIT window in the spectrum, as illustrated in Fig. 10(c).

When light is polarized along the y direction ($\theta = 90^\circ$), the two ribbon layers will exchange roles. That is, localized plasmon resonance in LLBPNRs can be directly excited, so they will work as bright mode. The ULBPNRs cannot directly interact with the incident light; thus, they will play the role of the dark mode. The one-way bright–dark mode interactions between the two ribbon layers directly lead to the PIT. Compared with the polarization perpendicular to the upper ZZ grating, the resonances for the polarization perpendicular to the lower AC grating shift to shorter wavelengths due to smaller effective mass along the AC direction. Interestingly, when the polarization is at an angle of 45° , plasmon resonances in both the ZZ and AC gratings can be excited at different positions simultaneously.

The directly excited plasmons in each layer will interact with the other layer in two separate coupling pathways, for which the resonant spectra will overlap and result in four absorption peaks with two transmission windows. Compared with the polarization perpendicular to the upper or lower ribbons, absorption intensity reduces at the respective plasmon resonance wavelengths due to a reduced light intensity in the corresponding x and y directions. Similar with BP layers, those absorption peaks indicate that, when the polarization is at an angle with the ribbons, both the upper- and lower-layer BPs work as bright and dark modes simultaneously at different resonant wavelengths. It is their two-way bright–dark mode couplings that lead to two transmission windows in the spectrum. Due to the anisotropic optical properties of BP, single- or double-window PIT effect can be achieved, depending on the polarization angle, as demonstrated by the absorption map shown in Fig. 10(b).

For the other two cases, that are with both the two ribbon layers constructed by ZZ and AC gratings, respectively. In each case, except for the orientation angle difference of 90° , all the related plasmonic parameters, including ribbon dimensions and dielectric constants (like effective mass and lattice orientation) along the ribbon edges, are the same. This is similar to the case with BP monolayers in the main text. Since there are always two bright modes or a bright mode and a dark mode simultaneously when the polarization is at an angle or perpendicular/parallel to the ribbon gratings, respectively, a transmission window is observed owing to either one-way bright–dark or bidirectional bright–bright and bright–dark modes hybridized couplings, as illustrated in Figs. 10(d)–10(i) for the two cases. As expected, these figures reveal that the characteristics of PIT spectra, including the absorption peaks and positions, spectra linewidths, time delay, and dielectric sensitivity, are completely insensitive to the polarization angle. Notably, we also have analytically fitted the absorption coefficient for the three cases using the two-particle model, finding excellent agreement between the two.

To further elucidate the coupling mechanism in BP, we plot the electric field distributions at the absorption peaks for all the cases in both the BP monolayers and nanoribbons in Fig. 11. Note that the symmetric mode (SM) corresponds to the resonance at a longer wavelength, while the antisymmetric mode (AM) relates to the resonance at a shorter wavelength. Firstly, for all the cases, the field distributions are highly dependent on the shape of BP and the surrounding dielectric material. Especially, the total electric field is more smoothly distributed in the

continuous BP sheet, while it is mostly pronounced around the edges in the patterned BPNR due to strong reflection at the edge. Besides, the field intensity in BPNR is much higher than that of the BP with dielectric gratings, indicating that patterned nanoribbons couple more efficiently with external light than the continuous BP monolayers. Despite this, the spatial distributions of the E_z components reveal the universality of the PIT effects. The in-phase and out-of-phase dipole mode couplings in the two layers directly lead to the symmetric and antisymmetric modes. To elaborate further, for all polarization directions, the directly excited bright mode will always retain its resonant phase along the polarization direction, while the dark mode will reverse its dipole signs at the AM.

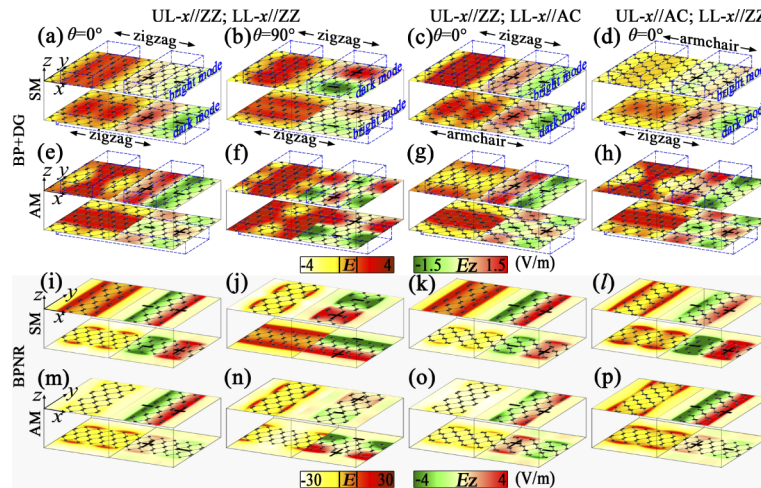


Fig. 11. Spatial distributions of the electric field (left panels) and the corresponding z component (right panels) of the SM (a-d, i-l) and AM (e-h, m-p) at polarization angles θ of 0° (except b, f, j, and n) and 90° (b, f, j, and n), which correspond to the designs with BP with dielectric gratings (BP + DG, a-h) in Figs. 8 and BP nanoribbons (BPNR, I-P) in Fig. 10, respectively. Signs “+” and “-” denote the oscillating surface charges; darker color represent higher charge density. Note that the same scalar bars are respectively used for all figures in the two situations.

Funding

National Natural Science Foundation of China (11904096, 11847230, 61775055, 61835004); China Postdoctoral Science Foundation (2018M642967).

Acknowledgment

The authors acknowledge Professor Tony Low for the access support of COMSOL Multiphysics.

Disclosures

The authors declare no conflicts of interest.

References

- W. L. Barnes, A. Dereux, and T. W. Ebbesen, “Surface plasmon subwavelength optics,” *Nature* **424**(6950), 824–830 (2003).
- F. J. García de Abajo, “Graphene Plasmonics: Challenges and Opportunities,” *ACS Photonics* **1**(3), 135–152 (2014).
- O. Nicoletti, F. de la Peña, R. K. Leary, D. J. Holland, C. Ducati, and P. A. Midgley, “Three-dimensional imaging of localized surface plasmon resonances of metal nanoparticles,” *Nature* **502**(7469), 80–84 (2013).

4. J. Chen, Y. Zeng, X. Xu, X. Chen, Z. Zhou, P. Shi, Z. Yi, X. Ye, S. Xiao, and Y. Yi, "Plasmonic Absorption Enhancement in Elliptical Graphene Arrays," *Nanomaterials* **8**(3), 175 (2018).
5. M. W. Knight, H. Sobhani, P. Nordlander, and N. J. Halas, "Photodetection with Active Optical Antennas," *Science* **332**(6030), 702–704 (2011).
6. A. N. Grigorenko, M. Polini, and K. S. Novoselov, "Graphene plasmonics," *Nat. Photonics* **6**(11), 749–758 (2012).
7. F. H. L. Koppens, T. Mueller, P. Avouris, A. C. Ferrari, M. S. Vitiello, and M. Polini, "Photodetectors based on graphene, other two-dimensional materials and hybrid systems," *Nat. Nanotechnol.* **9**(10), 780–793 (2014).
8. T. Low, A. Chaves, J. D. Caldwell, A. Kumar, N. X. Fang, P. Avouris, T. F. Heinz, F. Guinea, L. Martin-Moreno, and F. Koppens, "Polaritons in layered two-dimensional materials," *Nat. Mater.* **16**(2), 182–194 (2017).
9. Z. Sun, A. Martinez, and F. Wang, "Optical modulators with 2D layered materials," *Nat. Photonics* **10**(4), 227–238 (2016).
10. L. Han, L. Wang, H. Xing, and X. Chen, "Active Tuning of Midinfrared Surface Plasmon Resonance and Its Hybridization in Black Phosphorus Sheet Array," *ACS Photonics* **5**(9), 3828–3837 (2018).
11. X. Ni, L. Wang, J. Zhu, X. Chen, and W. Lu, "Surface plasmons in a nanostructured black phosphorus flake," *Opt. Lett.* **42**(13), 2659–2662 (2017).
12. D. N. Basov, M. M. Fogler, and F. J. García de Abajo, "Polaritons in van der Waals materials," *Science* **354**(6309), aag1992 (2016).
13. T. Low, R. Roldán, H. Wang, F. Xia, P. Avouris, L. M. Moreno, and F. Guinea, "Plasmons and Screening in Monolayer and Multilayer Black Phosphorus," *Phys. Rev. Lett.* **113**(10), 106802 (2014).
14. S. X. Xia, X. Zhai, Y. Huang, J. Q. Liu, L. L. Wang, and S. C. Wen, "Multi-band perfect plasmonic absorptions using rectangular graphene gratings," *Opt. Lett.* **42**(15), 3052–3055 (2017).
15. Y. Cai and K.-D. Xu, "Tunable broadband terahertz absorber based on multilayer graphene-sandwiched plasmonic structure," *Opt. Express* **26**(24), 31693–31705 (2018).
16. Y. Cai, K.-D. Xu, N. Feng, R. Guo, H. Lin, and J. Zhu, "Anisotropic infrared plasmonic broadband absorber based on graphene-black phosphorus multilayers," *Opt. Express* **27**(3), 3101–3112 (2019).
17. Y. Cai, J. Zhu, and Q. H. Liu, "Tunable enhanced optical absorption of graphene using plasmonic perfect absorbers," *Appl. Phys. Lett.* **106**(4), 043105 (2015).
18. M.-D. He, K.-J. Wang, L. Wang, J.-B. Li, J.-Q. Liu, Z.-R. Huang, L. Wang, L. Wang, W.-D. Hu, and X. Chen, "Graphene-based terahertz tunable plasmonic directional coupler," *Appl. Phys. Lett.* **105**(8), 081903 (2014).
19. M.-D. He, G. Zhang, J.-Q. Liu, J.-B. Li, X.-J. Wang, Z.-R. Huang, L. Wang, and X. Chen, "Plasmon resonances in a stacked pair of graphene ribbon arrays with a lateral displacement," *Opt. Express* **22**(6), 6680–6690 (2014).
20. K.-J. Wang, Y.-X. Peng, L. Wang, M.-D. He, Z.-J. Li, L.-H. Liu, J.-B. Li, X.-J. Wang, J.-Q. Liu, L. Xu, W.-D. Hu, and X. Chen, "Plasmon Resonances in a Periodic Square Coaxial Hole Array in a Graphene Sheet," *Plasmonics* **11**(4), 1129–1137 (2016).
21. L. Wang, X. Chen, A. Yu, Y. Zhang, J. Ding, and W. Lu, "Highly Sensitive and Wide-Band Tunable Terahertz Response of Plasma Waves Based on Graphene Field Effect Transistors," *Sci. Rep.* **4**(1), 5470 (2015).
22. G. Wang, S. Zhang, X. Zhang, L. Zhang, Y. Cheng, D. Fox, H. Zhang, J. N. Coleman, W. J. Blau, and J. Wang, "Tunable nonlinear refractive index of two-dimensional MoS₂, WS₂, and MoSe₂ nanosheet dispersions," *Photonics Res.* **3**(2), A51–A55 (2015).
23. K. L. Seyler, J. R. Schaibley, P. Gong, P. Rivera, A. M. Jones, S. Wu, J. Yan, D. G. Mandrus, W. Yao, and X. Xu, "Electrical control of second-harmonic generation in a WSe₂ monolayer transistor," *Nat. Nanotechnol.* **10**(5), 407–411 (2015).
24. S. X. Xia, X. Zhai, L. L. Wang, B. Sun, J. Q. Liu, and S. C. Wen, "Dynamically tunable plasmonically induced transparency in sinusoidally curved and planar graphene layers," *Opt. Express* **24**(16), 17886–17899 (2016).
25. L. Han, L. Wang, H. Xing, and X. Chen, "Anisotropic plasmon induced transparency in black phosphorus nanostrip trimer," *Opt. Mater. Express* **9**(2), 352–361 (2019).
26. S. Zhang, D. A. Genov, Y. Wang, M. Liu, and X. Zhang, "Plasmon-Induced Transparency in Metamaterials," *Phys. Rev. Lett.* **101**(4), 047401 (2008).
27. B. Peng, ŞK Özdemir, W. Chen, F. Nori, and L. Yang, "What is and what is not electromagnetically induced transparency in whispering-gallery microcavities," *Nat. Commun.* **5**(1), 5082 (2014).
28. H. Cheng, S. Chen, P. Yu, X. Duan, B. Xie, and J. Tian, "Dynamically tunable plasmonically induced transparency in periodically patterned graphene nanostrips," *Appl. Phys. Lett.* **103**(20), 203112 (2013).
29. W. Tang, L. Wang, X. Chen, C. Liu, A. Yu, and W. Lu, "Dynamic metamaterial based on the graphene split ring high-Q Fano-resonator for sensing applications," *Nanoscale* **8**(33), 15196–15204 (2016).
30. X. Zhao, L. Zhu, C. Yuan, and J. Yao, "Tunable plasmon-induced transparency in a grating-coupled double-layer graphene hybrid system at far-infrared frequencies," *Opt. Lett.* **41**(23), 5470–5473 (2016).
31. H. Yan, T. Low, F. Guinea, F. Xia, and P. Avouris, "Tunable Phonon-Induced Transparency in Bilayer Graphene Nanoribbons," *Nano Lett.* **14**(8), 4581–4586 (2014).
32. S. X. Xia, X. Zhai, L. L. Wang, and S. C. Wen, "Plasmonically induced transparency in double-layered graphene nanoribbons," *Photonics Res.* **6**(7), 692–702 (2018).
33. S. Xiao, T. Wang, T. Liu, X. Yan, Z. Li, and C. Xu, "Active modulation of electromagnetically induced transparency analogue in terahertz hybrid metal-graphene metamaterials," *Carbon* **126**, 271–278 (2018).

34. C. Wu, A. B. Khanikaev, and G. Shvets, "Broadband Slow Light Metamaterial Based on a Double-Continuum Fano Resonance," *Phys. Rev. Lett.* **106**(10), 107403 (2011).
35. D. F. Phillips, A. Fleischhauer, A. Mair, R. L. Walsworth, and M. D. Lukin, "Storage of Light in Atomic Vapor," *Phys. Rev. Lett.* **86**(5), 783–786 (2001).
36. H. Xu, M. Zhao, M. Zheng, C. Xiong, B. Zhang, Y. Peng, and H. Li, "Dual plasmon-induced transparency and slow light effect in monolayer graphene structure with rectangular defects," *J. Phys. D: Appl. Phys.* **52**(2), 025104 (2019).
37. S. Thongrattanasiri, A. Manjavacas, and F. J. García de Abajo, "Quantum Finite-Size Effects in Graphene Plasmons," *ACS Nano* **6**(2), 1766–1775 (2012).
38. M. Wurm, J. Endres, J. Probst, M. Schoengen, A. Diener, and B. Bodermann, "Metrology of nanoscale grating structures by UV scatterometry," *Opt. Express* **25**(3), 2460–2468 (2017).
39. M. B. Lundeberg, Y. Gao, R. Asgari, C. Tan, B. Van Duppen, M. Autore, P. Alonso-González, A. Woessner, K. Watanabe, T. Taniguchi, R. Hillenbrand, J. Hone, M. Polini, and F. H. L. Koppens, "Tuning quantum nonlocal effects in graphene plasmonics," *Science* **357**(6347), 187–191 (2017).
40. F. Meng, Q. Wu, D. Erni, K. Wu, and J. Lee, "Polarization-Independent Metamaterial Analog of Electromagnetically Induced Transparency for a Refractive-Index-Based Sensor," *IEEE Trans. Microwave Theory Tech.* **60**(10), 3013–3022 (2012).
41. S.-X. Xia, X. Zhai, L.-L. Wang, and S.-C. Wen, "Polarization-independent plasmonic absorption in stacked anisotropic 2D material nanostructures," *Opt. Lett.* **45**(1), 93–96 (2020).
42. S. X. Xia, X. Zhai, L. L. Wang, G. D. Liu, and S. C. Wen, "Excitation of surface plasmons in sinusoidally shaped graphene nanoribbons," *J. Opt. Soc. Am. B* **33**(10), 2129–2134 (2016).
43. L. Ju, B. Geng, J. Horng, C. Girit, M. Martin, Z. Hao, H. A. Bechtel, X. Liang, A. Zettl, Y. R. Shen, and F. Wang, "Graphene plasmonics for tunable terahertz metamaterials," *Nat. Nanotechnol.* **6**(10), 630–634 (2011).
44. Z. Fang, Y. Wang, A. E. Schlather, Z. Liu, P. M. Ajayan, F. J. García de Abajo, P. Nordlander, X. Zhu, and N. J. Halas, "Active Tunable Absorption Enhancement with Graphene Nanodisk Arrays," *Nano Lett.* **14**(1), 299–304 (2014).
45. S. Balci, O. Balci, N. Kakenov, F. B. Atar, and C. Kocabas, "Dynamic tuning of plasmon resonance in the visible using graphene," *Opt. Lett.* **41**(6), 1241–1244 (2016).
46. W. Gao, J. Shu, C. Qiu, and Q. Xu, "Excitation of Plasmonic Waves in Graphene by Guided-Mode Resonances," *ACS Nano* **6**(9), 7806–7813 (2012).
47. Y. Wang, T. Li, and S. Zhu, "Graphene-based plasmonic modulator on a groove-structured metasurface," *Opt. Lett.* **42**(12), 2247–2250 (2017).
48. Y. V. Bludov, N. M. R. Peres, and M. I. Vasilevskiy, "Graphene-based polaritonic crystal," *Phys. Rev. B* **85**(24), 245409 (2012).
49. S. Xia, X. Zhai, Y. Huang, J. Liu, L. Wang, and S. Wen, "Graphene Surface Plasmons With Dielectric Metasurfaces," *J. Lightwave Technol.* **35**(20), 4553–4558 (2017).
50. A. J. Chaves, N. M. R. Peres, D. R. da Costa, and G. A. Farias, "Channel surface plasmons in a continuous and flat graphene sheet," *Phys. Rev. B* **97**(20), 205435 (2018).
51. T. M. Slipchenko, M. L. Nesterov, L. Martin-Moreno, and A. Y. Nikitin, "Analytical solution for the diffraction of an electromagnetic wave by a graphene grating," *J. Opt.* **15**(11), 114008 (2013).
52. P. A. Huidobro, M. Kraft, S. A. Maier, and J. B. Pendry, "Graphene as a Tunable Anisotropic or Isotropic Plasmonic Metasurface," *ACS Nano* **10**(5), 5499–5506 (2016).
53. A. Ferreira and N. M. R. Peres, "Complete light absorption in graphene-metamaterial corrugated structures," *Phys. Rev. B* **86**(20), 205401 (2012).
54. Z. Li, Y. Xiao, Y. Gong, Z. Wang, Y. Kang, S. Zu, P. M. Ajayan, P. Nordlander, and Z. Fang, "Active Light Control of the MoS₂ Monolayer Exciton Binding Energy," *ACS Nano* **9**(10), 10158–10164 (2015).
55. R. Verre, D. G. Baranov, B. Munkhbat, J. Cuadra, M. Käll, and T. Shegai, "Transition metal dichalcogenide nanodisks as high-index dielectric Mie nanoresonators," *Nat. Nanotechnol.* **14**(7), 679–683 (2019).
56. W. Ma, P. Alonso-González, S. Li, A. Y. Nikitin, J. Yuan, J. Martín-Sánchez, J. Taboada-Gutiérrez, I. Amenabar, P. Li, S. Vélez, C. Tollan, Z. Dai, Y. Zhang, S. Sriram, K. Kalantar-Zadeh, S.-T. Lee, R. Hillenbrand, and Q. Bao, "In-plane anisotropic and ultra-low-loss polaritons in a natural van der Waals crystal," *Nature* **562**(7728), 557–562 (2018).
57. Z. Liu and K. Aydin, "Localized Surface Plasmons in Nanostructured Monolayer Black Phosphorus," *Nano Lett.* **16**(6), 3457–3462 (2016).
58. F. Xia, H. Wang, D. Xiao, M. Dubey, and A. Ramasubramaniam, "Two-dimensional material nanophotonics," *Nat. Photonics* **8**(12), 899–907 (2014).
59. D. Pan, R. Yu, H. Xu, and F. J. García de Abajo, "Topologically protected Dirac plasmons in a graphene superlattice," *Nat. Commun.* **8**(1), 1243 (2017).
60. D. Correas-Serrano, J. S. Gomez-Díaz, A. A. Melcon, and A. Alù, "Black phosphorus plasmonics: anisotropic elliptical propagation and nonlocality-induced canalization," *J. Opt.* **18**(10), 104006 (2016).
61. F. H. L. Koppens, D. E. Chang, and F. J. García de Abajo, "Graphene Plasmonics: A Platform for Strong Light–Matter Interactions," *Nano Lett.* **11**(8), 3370–3377 (2011).
62. Z. Fang, S. Thongrattanasiri, A. Schlather, Z. Liu, L. Ma, Y. Wang, P. M. Ajayan, P. Nordlander, N. J. Halas, and F. J. García de Abajo, "Gated Tunability and Hybridization of Localized Plasmons in Nanostructured Graphene," *ACS Nano* **7**(3), 2388–2395 (2013).